Assigning ionic properties in perovskite solar cells; a unifying transient simulation/experimental study

Mathias Fischer, David Kiermasch, Lidon Gil Escrig, Henk J. Bolink, Vladimir Dyakonov, and Kristofer Tvingstedt
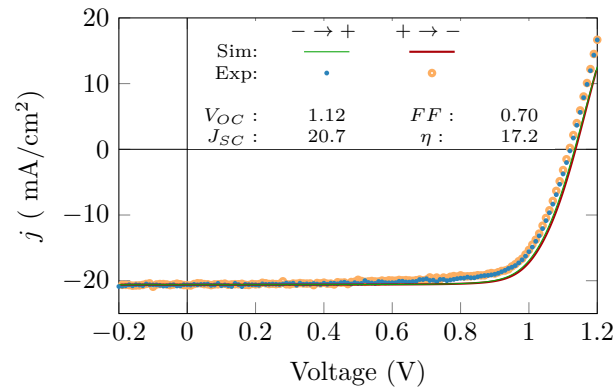
Supporting Information

FIG. S1: Measured and simulated $j(V)$ at 1 Sun light exposure, showing a complete absence of hysteresis at a 200mV/s scan rate. A series resistance of 200 Ωmm^2 was assumed in the simulations.
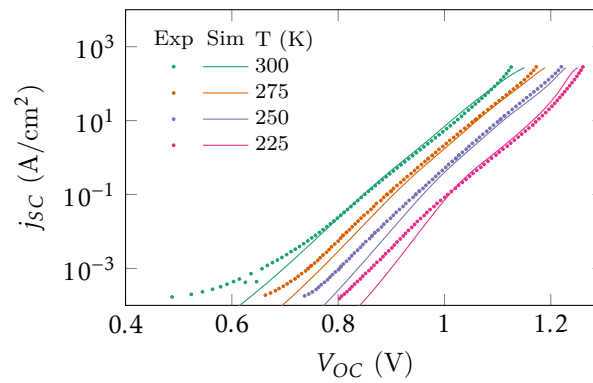

FIG. S2: Comparison of the measured and simulated $j_{SC}(V_{OC})$ relations.
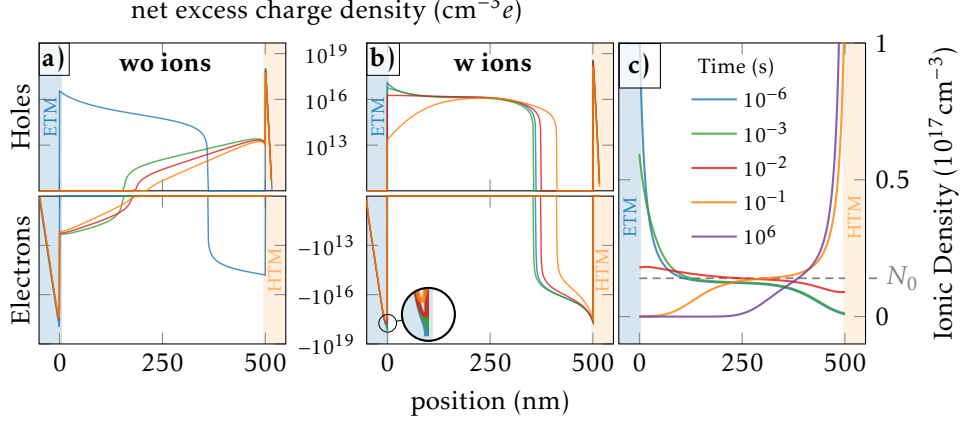
FIG. S3: Evolution of the net excess charge density during the simulated OCVD decay. a) Without mobile ions the charge density close to the ETM rises monotonically. b) Including mobile ions, where the increase of the net charge density left of the ETM/Perovskite interface is compensated by a decrease of the net charge density on the right of the ETM/Perovskite Interface, leading to an almost constant V_{OC}. c) The ionic density distribution.
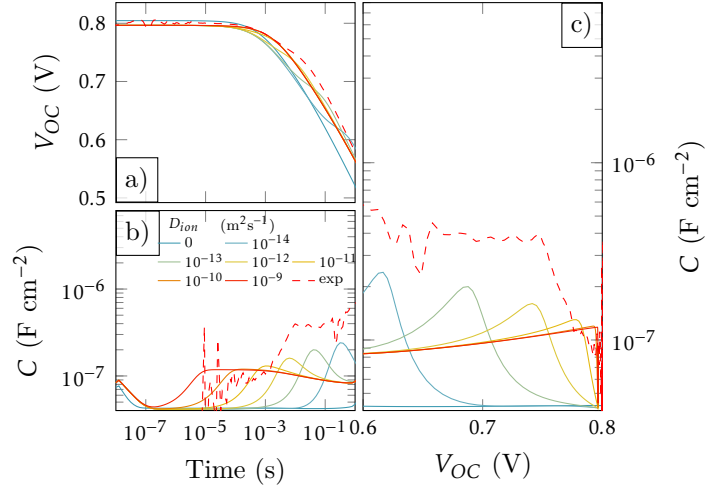

FIG. S4: Low perturbation measurement of a) OCVD, b) $C(t)$ and c) $C(V_{OC})$. leading to more accurate determination of D_{ion}.

A. Hysteresis

Especially in the case of only moderately or poorly performing perovskite solar cells, a hysteresis occurs in the IV characteristics in such a way that they differ depending on the

direction in which the voltage is swept through. In the presented method for the determination of ionic characteristics, IV-hysteresis is a challenge, since the total recombination rate in such a case is obviously also influenced by the internal ionic distribution. As a result, the recombination current obtained by IV measurement is not exactly the same as during OCVD. However, equation 2 shows that an error in the recombination current only contributes linearly to the determination of the capacitance, and thus has only a linear effect on the determination of the ion density. Therefore, if there is a low percentage of uncertainty in the recombination current due to hysteresis, this does not play a significant role for most practical concerns.

However, if the solar cell is excessively affected by hysteresis, it is advisable to use a variable scan rate instead of a fixed one. Ideally, the voltage during measurement would be run through at the same rate as it falls in the OCVD, so that an $j(V_{OC}(t))$ curve is obtained where the $V_{OC}(t)$ corresponds to the OCVD decay.

B. Numerical method

1. Model formulation

In a homogeneous thin-film solar cell where the device area is magnitudes larger than the thickness, it is sufficient to consider only the out of plane dimension. The electrons n, holes p, and ionic species P obey the conservation laws listed below. The respective current densities j_n, j_p and j_{ion} are composed of diffusion and field driven components, whereby the electric field is provided by the Poisson equation.

$$\frac{\partial n}{\partial t} = \frac{1}{q}\frac{\partial j_n}{\partial x} + G - R, \qquad\qquad j_n = qD^- \left(\frac{\partial n}{\partial x} - \frac{n\,q}{k_B T}\frac{\partial \phi}{\partial x}\right) \qquad (1)$$

$$\frac{\partial p}{\partial t} = \frac{-1}{q}\frac{\partial j_p}{\partial x} + G - R, \qquad\qquad j_p = -qD^+ \left(\frac{\partial p}{\partial x} + \frac{p\,q}{k_B T}\frac{\partial \phi}{\partial x}\right) \qquad (2)$$

$$\frac{\partial P}{\partial t} = \frac{-1}{q}\frac{\partial j_{ion}}{\partial x}, \qquad\qquad j_{ion} = -qD_{ion} \left(\frac{\partial P}{\partial x} + \frac{P\,q}{k_B T}\frac{\partial \phi}{\partial x}\right) \qquad (3)$$

$$0 = \frac{\partial^2 \phi}{\partial x^2} - \frac{q(N_{ion} - P + n - p - d_n + d_p)}{\varepsilon_{P/E/H}} \qquad (4)$$

4

In case of the perovskite layer we assumed an absence of doping, so that $d_n = d_p = 0$. D^- and D^+ are the corresponding diffusion coefficients and can be found in table 1 in the main text. For neutrality reasons the Poisson equation must also contain the immobile counterpart of the mobile ionic species, which is assumed to be uniformly distributed in the perovskite layer. We note here that the Poisson equation does not contain any time derivative, which essentially excludes explicit time integration of the system whereby only implicit methods can be used to integrate the equations. Such partial differential-algebraic equations are solved by discretization of one variable. As the spatial domain is fixed by the device geometry, a discretization in this dimension is appropriate and conducted by the numerical scheme proposed by Courtier et al.[1,2]. We took their MATLAB implementation as a blueprint and translated it to Julia, a programming Language showing a performance comparable to C code when used correctly.[3] For the integration of the equations we used the Julia package DifferentailEquations.jl, developed by Rackauckas et al.[4]. The existence of this package was the main reason why we re-implemented Courtiers method. The package can handle colored jacobians[5] natively, uses forward-mode automatic differentiation[6], and provides high order, stiffness aware, implicit Rosendbrock integrators like the Rodas4P[7]. All this measures together allows us to simulate a whole OCVD from nano to mega seconds timescale on a grid out of 600 stencils with low relative (10^{-6}) and absolute (10^{-6}) tolerances on a standard desktop computer in less then one second.

2. *Transport layers*

For the transport layers simplified equations were applied. These specifically consisted of the assumptions that the HTM / ETM only conducts holes / electrons (n / $p = 0$) and no charge generation G and recombination R takes place, as well as there are no mobile ions present ($P = N_{ion} = 0$). As transport materials usually are wide bandgap materials and considered to be doped, its appropriate to only account for the majority carriers as justified by the mass action law for non degenerated semiconductors $np = n_i^2$. The intrinsic charge carrier density n_i is given by the effective electron and hole masses and the bandgap E_g:

$$n_i^2 = N_c \, N_v \cdot e^{-E_g/(k_B T)} \tag{5}$$

$$N_{c/v} = 2 \cdot (2\pi m_{n/p} k_B T / h^2)^{3/2} \tag{6}$$

5

where h is planck's constant. Equation 5 is stating that wide bandgap materials generally tend to have few intrinsic carriers so that it is reasonable to assume that for the ETM $d_n \approx n \gg n_i \Rightarrow n \ggg p$ holds, an analogous statement applies to the HTM. Equation 6 expresses the temperature dependence of the density of states within the free electron gas model.

As underlying mechanism of charge carrier exchange between transport layers and absorber material thermionic emission in detailed balance is assumed. As a result the ratio of charge carrier densities at both sides of the interface is treated as fixed by:

$$\frac{n_r}{n_l} = \frac{N_{cr}}{N_{cl}} \exp(\Delta E_E / k_B T) \tag{7}$$

$$\frac{p_l}{p_r} = \frac{N_{vl}}{N_{vr}} \exp(\Delta E_H / k_B T) \tag{8}$$

where $n_{l/r}/p_{l/r}$ and N_l/N_r indicating the carrier densities and effective density of states left/right of the interface if the layer sequence ETM-Perovskite-HTM is present.

3. Recombination model

The bulk recombination behavior in the simulations is composed of Schokley-Read-Hall, and bimolecular recombination

$$R(n,p) = \frac{(n \cdot p - n_i)}{\tau_p \cdot n + \tau_n \cdot p} + k_{rad} \cdot (n \cdot p - n_i) \tag{9}$$

For surface recombination, only Shockley-Read-Hall is assumed. Here, the charge carriers from the transport layers are assumed to recombine together with their opposite ones from the bulk. We also allow the surface recombination velocities ν_{p_E}, ν_{n_E} at the ETM/Perovskite interface to differ from ν_{p_H}, ν_{n_H} at the Perovskite/HTM interface.

$$R_{E/H}(n_{l/r}, p_{r/l}) = \frac{(n_{l/r} \cdot p_{r/l} - n_i)}{\nu_{p_{E/H}} \cdot n_{l/r} + \nu_{n_{E/H}} \cdot p_{r/l}} \tag{10}$$

4. Total current density

The total current density was calculated as:

$$J(t) = j_n - \varepsilon_E \frac{\partial^2 \phi}{\partial t \partial x} \tag{11}$$

6

as shown in[2]. In contrast to Courtier et al. we calculate the current density not in the middle of the active layer, but close to the outer edge of the ETL. This is due to the fact that the the PDE has much smoother solutions here than in bulk. The resulting low gradients in n and ϕ lead to less loss of significance in equation 1 and therefore reduced numerical errors. This is especially important in dark IV curves at low voltages where the current densities become very low.

C. Built in potential

The built-in potential is defined as the difference between the chemical potentials (Fermi level relative to the conduction/valence-band-minimum) of the respective transport layers in the dark. It depends therefore not only on the conduction (E_C)/valence (E_V) band energy levels themselves but also on the electron(n)/hole(p) density present in the layers.

$$n = N_c e^{\frac{E_{F_n} - E_C}{k_B T}} \qquad \longleftrightarrow \qquad E_{F_n} = k_B T \, \log(n/N_C) + E_C \qquad (12)$$

$$p = N_v e^{\frac{E_V - E_{F_p}}{k_B T}} \qquad \longleftrightarrow \qquad E_{F_p} = -k_B T \, \log(p/N_V) + E_V \qquad (13)$$

where N_C/N_V corresponds to the effective densities of the conduction/valence band states, respectively as defined in equation 6. In the transport layers the electron end hole densities are equal the effective doping densities n_E/p_H and we get V_{BI}:

$$V_{BI} = E_{F_{ETM}} - E_{F_{HTM}} \qquad (14)$$

$$= (k_B T \, \log(n_E/N_{C_{ETM}}) + E_{C_{ETM}}) - (-k_B T \, \log(p_H/N_{V_{HTM}}) + E_{V_{HTM}}) \qquad (15)$$

$$= +k_B T \, \log(\frac{n_E \cdot p_H}{N_{C_{ETM}} \cdot N_{V_{HTM}}}) + E_{C_{ETM}} - E_{V_{HTM}} \qquad (16)$$

This does also mean that the V_{BI} is ruled by the band energies but more important also by the doping density. For the values in our simulation from Table 1 this evaluates to 0.987 eV.

D. Solar cell fabrication

The co-evaporated planar PIN sample was manufactured according to the description outlined in reference[8]:

Materials: Photolithographically patterned ITO coated glass substrates were purchased from Naranjo Substrates. 2,2'-(Perfluoronaphthalene-2,6-diylidene)dimalononitrile (F6-TCNNQ), N4,N4,N4"-tetra([1,1'-biphenyl]-4-yl)[1,1':4',1"-terphenyl]-4,4"-diamine (TaTm) and N1,N4-bis(tri-p-tolylphosphoranylidene)benzene-1,4-diamine (PhIm) were provided from Novaled GmbH. Fullerene (C_{60}) was purchased from Sigma Aldrich. PbI_2 was purchased from Tokyo Chemical Industry CO (TCI), and CH_3NH_3I (MAI) from Lumtec.

Preparation of the n-i-p devices: ITO-coated glass substrates were subsequently cleaned with soap, water and isopropanol in an ultrasonic bath, followed by UV-ozone treatment. They were transferred to a vacuum chamber integrated into a nitrogen-filled glovebox (MBraun, H_2O and $O_2 < 0.1$ ppm) and evacuated to a pressure of $1 \cdot 10^{-6}$ mbar. The vacuum chamber is equipped with six temperature-controlled evaporation sources (Creaphys) fitted with ceramic crucibles. The sources were directed upwards with an angle of approximately 90° with respect to the bottom of the evaporator. The substrate holder to evaporation sources distance is approximately 20 cm. Three quartz crystal microbalance (QCM) sensors are used, two monitoring the deposition rate of each evaporation source ad a third one close to the substrate holder monitoring the total deposition rate. For thickness calibration, we first individually sublimed the charge transport materials and their dopants (TaTm and F6-TCNNQ, C_{60} and PhIm). A calibration factor was obtained by comparing the thickness inferred from the QCM sensors with that measured with a mechanical profilometer (Ambios XP1). Then these materials were co-sublimed at temperatures ranging from 135-160 °C for the dopants to 250 °C for the pure charge transport molecules, and the evaporation rates was controlled by separate QCM sensors and adjusted to obtain the desired doping concentration. In general, the deposition rate for TaTm and C_{60} was kept constant at 0.8 Å/s while varying the deposition rate of the dopants during co-deposition. Pure TaTm and C_{60} layers were deposited at a rate of 0.5 Å/s. For this n-i-p configuration, 40 nm of the n-doped electron-transport layer (n-ETL, C_{60}:PhIm) capped with 10nm of the pure C_{60} were deposited. Once completed this deposition, the chamber was vented with dry N_2 to replace the 3–ETL crucibles with those containing the starting materials for the perovskite deposition, PbI_2 and CH_3NH_3I. The vacuum chamber was evacuated again to a pressure of 10^{-6} and the perovskite films were then obtained by co-deposition of the two precursors. The calibration of the deposition rate for the CH_3NH_3I was found to be difficult due to non-uniform layers and the soft nature of the materials which impede accurate thickness

measurements. Hence, during the evaporation the rate of the CH_3NH_3I was kept at 1 Å/s and the rate of the PbI_2 was kept at 0.5 Å/s. These rates were adjusted by grazing incident x-ray diffraction. After deposition of the perovskite film, the chamber was vented, and the crucibles replaced with those containing TaTm and F6-TCNNQ and evacuated again to a pressure of 10-6 mbar. The devices were completed depositing a film of pure TaTm and one of the p-HTL (TaTm: F6-TCNNQ), with a thickness of 10 and 40 nm, respectively. Finally, the substrates were transferred to a second vacuum chamber where the metal top contact (100 nm thick) was deposited.

E.   Experimental method

The OCVD measurements were conducted by illuminating the cell with a high power spectrally stable cold LED (Seoul) for 2 seconds, to then rapidly switch it off; employing a home built electrical switch and an Agilent 81150A function generator. For our studied device, the 2 seconds was always enough to reach steady state conditions at 300K but perhaps not sufficient at temperatures below 200K as outlined in the main text, but we are aware of that this may not be the case for a majority of perovskite devices. The voltage decay of the solar cells, over a 1 TΩ input impedance amplifier (Femto Messtechnik GmbH), was monitored by an Agilent Infinium 90254A digital storage oscilloscope. This high load of the measurement instrumentation is crucial, as it will otherwise have the same effect as having a leaky shunt resistor in parallel with the device[9]. Accordingly, if one intends to correctly monitor the voltage decay of the cell only, the measurement load needs to be as high as possible.

References

[1] N. E. Courtier, J. M. Cave, J. M. Foster, A. B. Walker, G. Richardson, *Energy & Environmental Science* **2019**, *12*, 1 396.

[2] N. E. Courtier, J. M. Cave, A. B. Walker, G. Richardson, J. M. Foster, *Journal of Computational Electronics* **2019**, *18*, 4 1435.

[3] J. Bezanson, A. Edelman, S. Karpinski, V. B. Shah, *SIAM Review* **2017**, *59*, 1 65.

[4] C. Rackauckas, Q. Nie, *Journal of Open Research Software* **2017**, *5*.

[5] A. H. Gebremedhin, F. Manne, A. Pothen, *SIAM Review* **2005**, *47*, 4 629.

[6] J. Revels, M. Lubin, T. Papamarkou, *arXiv:1607.07892 [cs.MS]* **2016**.

[7] G. Steinebach, *Order-reduction of ROW-methods for DAEs and method of lines applications*, volume 1741, Techn. Hochschule, Darmstadt, **1995**.

[8] D. Kiermasch, L. Gil-Escrig, A. Baumann, H. J. Bolink, V. Dyakonov, K. Tvingstedt, *J. Mater. Chem. A* **2019**, *7* 14712.

[9] K. Tvingstedt, L. Gil-Escrig, C. Momblona, P. Rieder, D. Kiermasch, M. Sessolo, A. Baumann, H. J. Bolink, V. Dyakonov, *ACS Energy Letters* **2017**, *2*, 2 424.